Engineering Solid Mechanics 13 (2025) 165-174

Contents lists available at GrowingScience

Engineering Solid Mechanics

homepage: www.GrowingScience.com/esm

Piezoelectric patch-based metamaterial on thin plates with arrays of separately shunted patches-validation and optimization

Mustafa Kemal Acar[a] and Peyman Lahe Motlagh[a*]

[a]*Department of Mechanical Engineering, Gebze Technical University, Kocaeli, Turkey*

ARTICLEINFO

Article history:
Received 10 July 2024
Accepted 15 January 2025
Available online
15 January 2025

Keywords:
Electromechanical systems
Shunt damping
Thin plate structures
Rayleigh-Ritz model
Piezoelectric patches

ABSTRACT

Lightweight structures tend to be susceptible to vibration, which can lead to fatigue and failure. Piezoelectric shunt damping is an efficient technology that converts mechanical energy into electrical energy and dissipates it through shunt circuits without requiring external power. This study models several piezoelectric patches coupled to different shunt circuits on a thin plate, utilizing Rayleigh-Ritz modal analysis to examine patch parameters including size, position, and distribution. Optimization demonstrates that effective patch-circuit topologies correspond with structural mode shapes, resulting in maximum vibration reduction. The findings introduce a fresh technique to enhance vibration control which improves structural reliability and performance.

1. Introduction

Modern high-speed, lightweight structures are becoming more susceptible to significant vibrations as a result of their design and functional properties. These vibrations can significantly reduce the structural lifespan by accelerating material fatigue and degradation (Dekemele et al., 2024). Additionally, they pose a considerable risk of mechanical failure, potentially leading to catastrophic consequences in various engineering applications. The need for advanced vibration control and mitigation strategies is thus critical to ensure the safety, reliability, and durability of these structures (Zhang et al., 2024). Throughout the years, a wide range of semi-passive and passive solutions have been advocated for decreasing these vibrations (Erturk & Inman, 2011). Piezoelectric shunt damping is a commonly employed method for reducing vibrations in smart structures. Piezoelectric transducers (PZTs), when paired with the proper electronic circuits, can function as devices to dissipate mechanical energy (Muthalif & Wahid, 2021). By converting mechanical vibrations or stress into electrical energy, which can then be managed or dissipated through the circuitry, these PZTs serve a critical role in reducing unwanted mechanical energy in various systems (Richardt et al., 2024). They can also ensure the stability of the system with the shunt, and they do not rely on parametric models for the design process. This means that the methods can be implemented without requiring detailed mathematical models of the system's parameters, simplifying the design and implementation process while still providing stable operation. In addition to this, this approach allows for a compact method of damping vibrations that doesn't require adding much additional mass or taking up considerable space. By integrating the system in this way, effective vibration control is achieved without compromising the overall weight or the spatial efficiency of the structure (Yaw et al., 2024). When a simple resistor is connected to the terminals of a piezoelectric transducer (PZT), the PZT functions similarly to a viscoelastic damper. When the network incorporates a series inductor-resistor (R-L) circuit, the passive elements, combined with the intrinsic capacitance of the PZT, generate a damped electrical resonance (Fleming & Moheimani, 2003). The resonance can be tuned to allow the PZT to operate as a vibrational energy absorber with specific frequency targeting.

Shunt circuits operate without the need for a feedback sensor to monitor or adjust their performance (Liao et al., 2024; Motlagh et al., 2018). In some cases, these circuits can function effectively without the need for any supplementary electronic components or an external power supply (Ma et al., 2024). This makes them particularly advantageous in applications where

* Corresponding author.
E-mail addresses: peyman.lahe@gtu.edu.tr (P. L. Motlagh)

ISSN 2291-8752 (Online) - ISSN 2291-8744 (Print)

doi: 10.5267/j.esm.2025.1.003

simplicity, reliability, and low maintenance are important, as they can achieve their purpose without the added complexity of additional equipment (Paixão et al., 2024). Piezoelectric materials are most commonly utilized in the form of patches or layers by being integrated onto the surfaces of structures that are flexible and resemble beams or plates (Acar & Motlagh, 2024; Aghakhani et al., 2019; Lahe Motlagh et al., 2023; Motlagh et al., 2020). To control vibrations, piezoelectric transducers are attached to the base structure using a strong adhesive material (Lahe Motlagh et al., 2023). Piezoelectric transducers have the capability to serve as sensors, actuators, or a combination of both. In a common active control application, a piezoelectric transducer functions as an actuator (Gardonio & Rodrigues, 2024; Motlagh et al., 2021). A sensor is employed to detect the vibrations in the base structure, and a control voltage is then applied to the piezoelectric actuator to reduce or eliminate the unwanted vibrations in the structure.

To the best of my knowledge of authors, there isn't any significant modeling of separated circuits for shunt damping purposes, so to fill the gap, this paper tries to showcase various shunt circuits attached to a system of piezoelectric patches on a thin plate. The most important novelty of the current paper is the usage of a high number of patches attached to different circuits and integrated to a thin plate. To model the effect of patches, Rayleigh-Ritz assumptions are used to perform the modal analysis and by varying the size parameters such as patch locations, dimensions and ratio compared to plate, efficiency of the current model is shown. A brute-force through optimization is performed to show the best patch-circuit configuration to achieve highest shunt performance and it is shown that patch-circuit distribution follows the same trend as mode shapes.

2. A model of independent piezoelectric patches a plate

This section provides a concise overview of the methodology employed in the paper, as illustrated in **Fig. 1**., the patches are a system of grid scattering all over the plate and each has its own unique circuit and thus it can act independently compared to other patches.

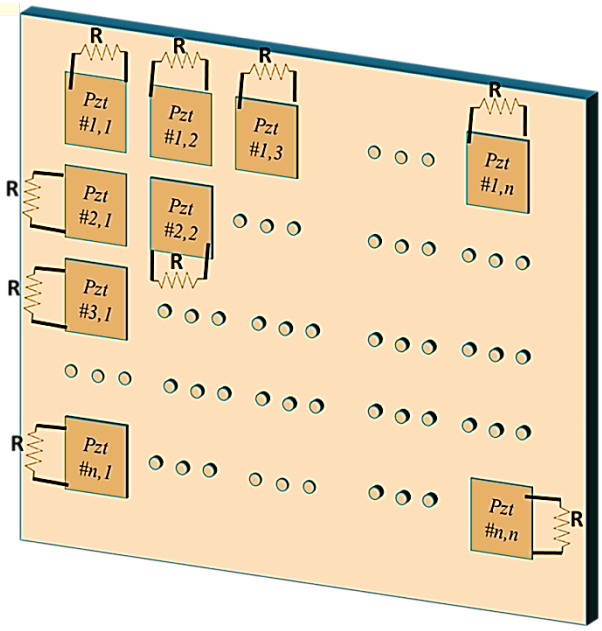

Fig. 1. Schematic of the distinct arrangement of the piezoelectric patches in relation to the base plate

Hamilton's principle is utilized to derive the governing equation of motion:

$$\delta \oint_{t_1}^{t_1} (T - U + W_p)\, dt = 0 \tag{1}$$

Externally applied work, potential energy and kinetic energy are denoted as *U, T,* and W_p, respectively (Marion, 2013). *P(x,y)* function is introduced to delineate the regions at which k piezoelectric patches are affixed onto the structural layer's surface as follows:

$$F(x,y) = \sum_{i=1}^{k} \left[H\left(x - x_{i,1}\right) - H(x - x_{i,2})\right] \times \left[H\left(y - y_{i,1}\right) - H(y - y_{i,2})\right] \tag{2}$$

Here, y_1, y_2, x_1 *and* x_2, represent the coordinates of the points on edge of x and y axis and *H* refers to the Heaviside function. The corresponding is expressed as:

$$m(x,y) = \rho_s h_s + \rho_p h_p F(x,y) \tag{3}$$

The capacitance C_p^k of the k^{th} piezoelectric patch is characterized by Equ. (4): :

$$C_p{}^k = \int_{S_p} \frac{\varepsilon^S{}_{33}}{h_p} dS_p \tag{2}$$

The Kirchhoff's laws can be utilized in electrical circuits to derive Eq. (5). Eq. (4) with Eq. (5) is compared and the current flowing through the k^{th} piezoelectric patch is expressed as Eq. (6) (Erturk & Inman, 2009).

$$C_p{}^k \left(\frac{dv(t)}{dt}\right) + \frac{v(t)}{Z_l} = i_k(t) \tag{3}$$

$$i_k(t) = -\bar{e}_{31}\left(\frac{h_p + h_s}{2} - z_0\right)\frac{\partial}{\partial t} \int_{S_p} \nabla^2 w(x,y,t) dS_p \tag{4}$$

Subsequently, the present result in modal coordinates can be determined by inserting into Eq. (6), resulting in the following expression:

$$i_k(t) = -\sum_{n=1}^{N}\sum_{r=1}^{R} \frac{d\eta_{rn}(t)}{dt} \tilde{\theta}_{rn}{}^k \tag{5}$$

Here, $\tilde{\theta}_{rn}{}^k$ is defined by Eq. (8):

$$\tilde{\theta}_{rn}{}^k = -\bar{e}_{31}\left(\frac{h_p + h_s}{2} - z_0\right)\int_{S_p} U_{rn}\nabla^2 W_{rn}(x,y) dS_p \tag{6}$$

Assuming that the transverse force excitation on the host plate is harmonic and given by $f(t)=F_0 e^{j\omega t}$ (where F_0 represents the force amplitude and ω denotes the excitation frequency), the linear system assumption indicates that the mechanical and electrical responses can be expressed as harmonic functions: $\eta_{rn}(t)=H_{rn}e^{j\omega t}$ and $v_k(t)=V_k e^{j\omega t}$, respectively.

In the isolated arrangement, every patch is linked to its own electrical circuit independently, similar to what is shown in **Fig. 1.** The circuit equation can be stated as Eq. (9) using Kirchhoff's current law for each patch,

$$C_p{}^k \left(\frac{dv_k(t)}{dt}\right) + \frac{v_k(t)}{(Z_l)_k} = i_k(t), (k = 1,2,\dots, Number\ of\ patches) \tag{9}$$

The distinct differential equations of motion in modal coordinates were established earlier in (Erturk and Inman, 2009) and (Yoon et al., 2016), represented as Eq. (10), where the voltage $v_k(t)$ varies for each patch:

$$\frac{d^2\eta_{rn}(t)}{dt^2} + 2\omega_{rn}\xi_{rn}\frac{d\eta_{rn}(t)}{dt} + \omega_{rn}{}^2\mu_{rn}(t) - \sum_{k=1}^{K}\theta_{rn}{}^k v_k(t) = f_{rn}(t) \tag{10}$$

where $f_{rn}(t)$ (Yoon et al., 2016) is defined as:

$$f_{rn}(t) = f(t)\, U_{rn} W_{rn}(x_0, y_0) \tag{11}$$

Based on Eq. (7) and Eq. (9), the connection between voltage $V_k(t)$ and W_{rn} can be expressed as Eq. (12):

$$\left[\frac{1}{(Z_l)_k} + j\omega C_p{}^k\right] V_k(t) + j\omega \sum_{n=1}^{N}\sum_{r=1}^{N} \frac{F_0 U_{ij} W_{ij}(x_0,y_0)\tilde{\theta}_{ij}{}^k}{\omega_{ij}{}^2 - \omega^2 + (2j)\xi_{ij}\omega_{ij}\omega} + j\omega \sum_{i=1}^{N}\sum_{j=1}^{N} \tilde{\theta}_{ij}{}^k \frac{\sum_{k=1}^{k}\tilde{\theta}_{ij}{}^k v_k(t)}{\omega_{ij}{}^2 - \omega^2 + (2j)\xi_{ij}\omega_{ij}\omega} = 0. \tag{12}$$

Thus, this equation's only variables are voltage $V_k(t)$, and they can be identified as follows:

$$\begin{bmatrix} V_1 \\ \vdots \\ V_k \\ \vdots \\ V_n \end{bmatrix} = A^{-1} \begin{bmatrix} b_1 \\ \vdots \\ b_k \\ \vdots \\ b_n \end{bmatrix} \tag{13}$$

where A is defined as Eq. (14) :

$$A = \begin{bmatrix} \left\{\frac{1}{(Z_l)_1} + j\omega {C_p}^1 + {a'}_{11}\right\} & \cdots & {a'}_{1k} & \cdots & {a'}_{1n} \\ \vdots & \ddots & \ddots & \ddots & \vdots \\ {a'}_{k1} & \ddots & \left\{\frac{1}{(Z_l)_k} + j\omega {C_p}^k + {a'}_{kk}\right\} & \ddots & {a'}_{kn} \\ \vdots & \ddots & \ddots & \ddots & \vdots \\ {a'}_{n1} & \cdots & {a'}_{nk} & \cdots & \left\{\frac{1}{(Z_l)_n} + j\omega {C_p}^n + {a'}_{nn}\right\} \end{bmatrix} \quad (14)$$

where $a\ and\ b$' are defined as

$$a'_{ls} = j\omega \sum_{j=1}^{N} \sum_{i=1}^{N} \frac{\tilde{\theta}_{ij}{}^{l} \tilde{\theta}_{ij}{}^{s}}{{\omega_{ij}}^2 - \omega^2 + 2j\xi_{ij}\omega_{ij}\omega}, (i,j = 1, \dots, N), (l,s = 1,2, \dots, number\ of\ patches) \quad (15)$$

$$b_k = j\omega \sum_{i=1}^{N} \sum_{j=1}^{N} \frac{F_0 U_{ij} W_{ij}(x_0, y_0) \tilde{\theta}_{ij}{}^{k}}{{\omega_{rn}}^2 - \omega^2 + 2j\xi_{rn}\omega_{rn}\omega}, (k = 1,2, \dots, number\ of\ patches) \quad (16)$$

By determining $V = [v_1 \quad \cdots \quad v_k \quad \cdots \quad v_n]^T$ from Eq. (13) and substituting it into Eq. (10), the plate's relative displacement can be described as shown in Eq. (17):

$$w(x,y,t) = \sum_{i=1}^{N} \sum_{j=1}^{N} U_{ij}\, W_{ij}(x,y) \left\{ \frac{F_0 U_{ij} W_{ij}(x_0, y_0) + \sum_{k=1}^{K} \theta_{ij} A^{-1} [b_1 \quad \cdots \quad b_k \quad \cdots \quad b_n]^T}{{\omega_{ij}}^2 - \omega^2 + 2j\xi_{ij}\omega_{ij}\omega} \right\} e^{j\omega t} \quad (17)$$

3. Results and discussions

This section will present detailed electromechanical frequency response function (FRF) data for isolated setups, it will cover the overall performance of the current model by investigating different size, ratio and location of patches.

3.1 One patch configuration: changing thickness and area of the patch

This section includes investigation of the shunt damping performance via one patch which is located at the center of the plate. Fig. 2. represents a demonstration of the cases where the piezoelectric patch size is varied. The ratio of the patch thickness to the plate thickness $\frac{h_p}{h_s}$ varies from 0.1 to 0.9 and the area coverage ratio $\frac{A_p}{A_s}$ varies from 0.005 up to 0.75.

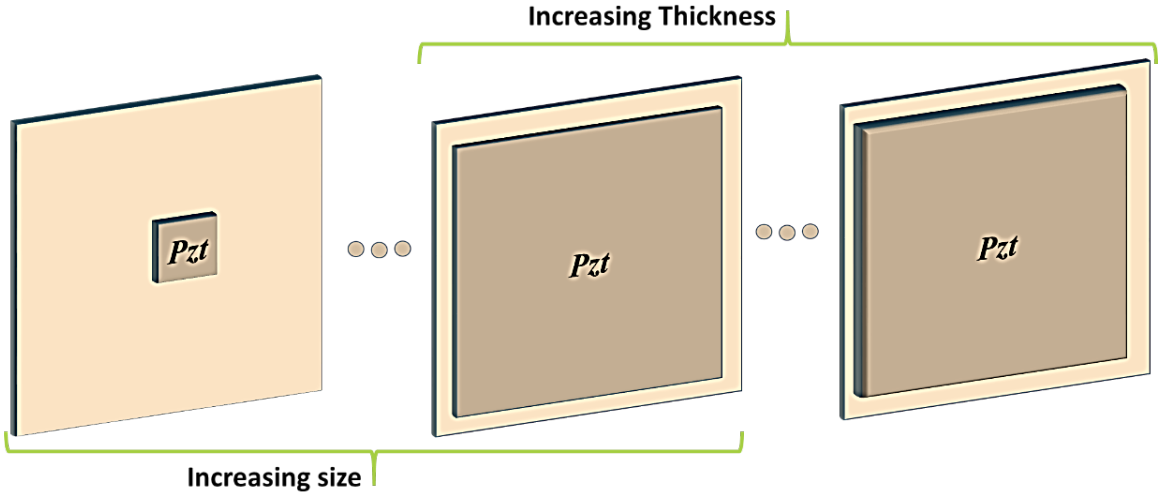

Fig. 2. Demonstration of increasing size and thickness of one patch configuration.

Fig. 3. shows the reduction percentage of the $\overline{\text{ERP}}$ on the first 6 modes of the system when the $\frac{h_p}{h_s}$ *and* $\frac{A_p}{A_s}$ values are varied. At every stage, the average energy recovery performance $\overline{\text{ERP}}$ is computed as the resistance value is changed from short circuit named as SC (R = 100 Ω) to open circuit named as OC (R = 1 MΩ). The optimal value for resistor R_{opt} is identified when the average $\overline{\text{ERP}}$ is at its lowest point. The same procedure is repeated at different thickness and area ratios and then the percent reduction is calculated**.**

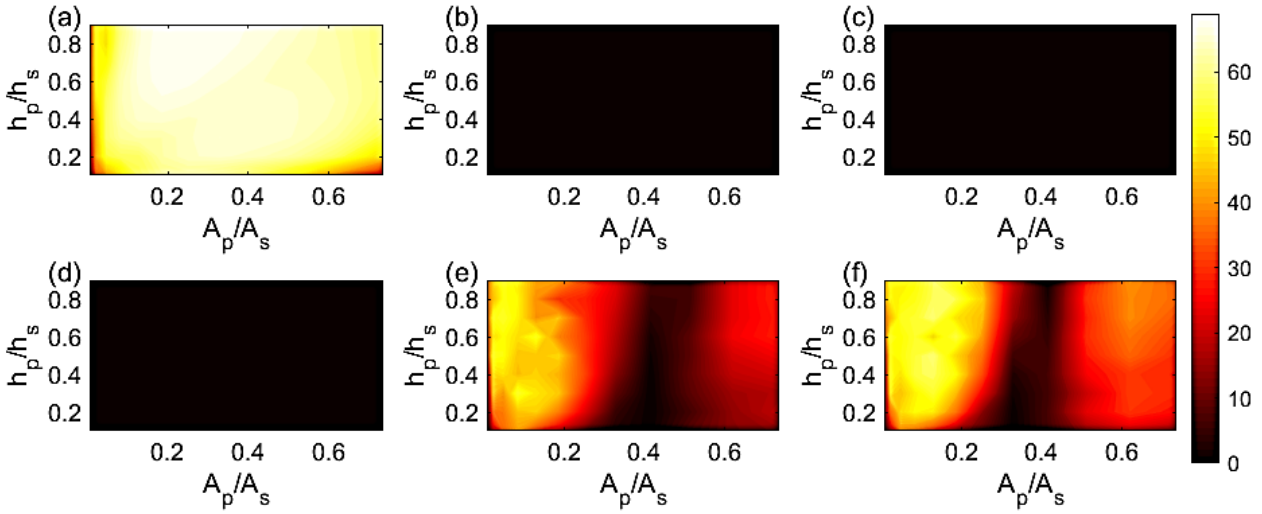

Fig. 3. Percent reduction in average energy recovery performance $\overline{\text{ERP}}$ for the first six modes using a single patch with an R shunted circuit: (a) First mode , (b) Second mode , (c) Third mode , (d) Fourth mode, (e) Fifth mode, and (f) Sixth mode ; the R values are consistent across all cases.

Fig. 3. shows that, due to the patch location and the strain mode shapes, $\overline{\text{ERP}}$ reduction in modes 2, 3 and 4 cannot be achieved. There is a black gap near $\frac{A_p}{A_s} = 0.36$ at modes 1, 5 and 6 which indicates that increasing the piezoelectric patch size has some negative-effect which could be linked to the cancelation of the piezoelectric effect due to the symmetry of the strain mode shapes. The maximum percent reduction is 69% and only achievable for the first mode.

3.2 Multiple patch configurations: changing thickness and number of the patches

This section investigates the $\overline{\text{ERP}}$ percent reduction for separated and connected configurations, **Fig. 4**. demonstrates how the number and thickness of the patches are varied. The location of the patches is adjusted while increasing the number of the patches in a symmetric pattern with respect to the middle axis of the plate. The patches are chosen with sizes $40 \times 40\ mm^2$ and the numbers of patches are increased from 1 to 144. When 144 patches are positioned on the plate, the area ratio of total patches to the area of the plate will be equal to 0.75 the same as the biggest patch in the previous section. The thickness ratio of the patches is also varied from 0.1 to 0.9, such that the results are comparable with the previous section.

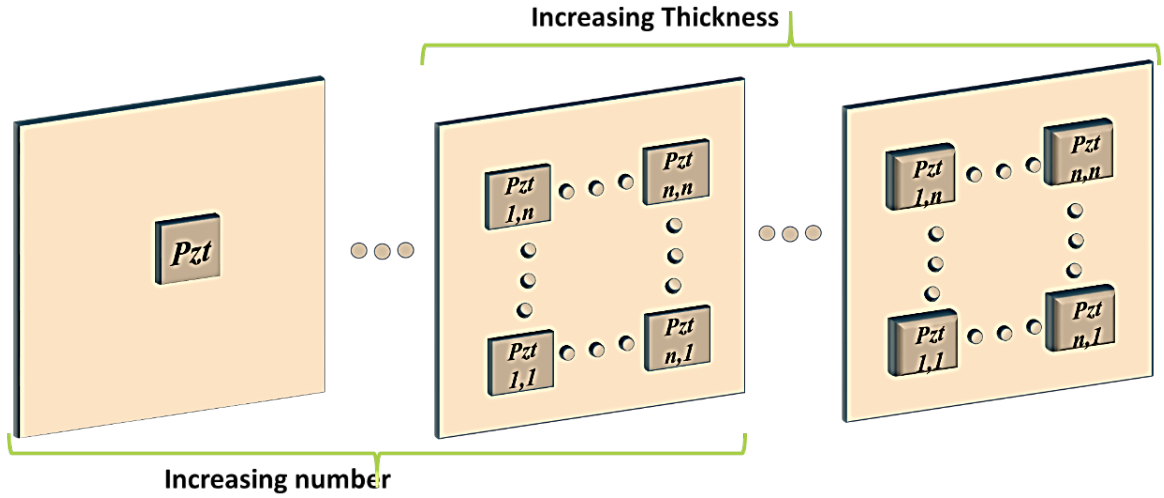

Fig. 4. Demonstration of increasing number and thickness of the multiple patches.

The percent reduction in average energy recovery performance $\overline{\text{ERP}}$ for both connected and separated configurations is shown in **Fig. 5**. At each stage, the average ERP is computed as the resistance value is adjusted from SC to OC. For different patch thicknesses, the same procedure is repeated. Fig. 5. shows that the shunt circuit in connected configuration is ineffective for modes 2, 3, and 4 as in the case of single patch configuration in the previous section. This result indicates that the connected patches work as one patch and make the Eq. (6) ineffective. When patch locations are symmetric relative to the middle axis of the plate, the percent reduction gets worse where the strain mode shape is also symmetric relative to the middle axis of the plate. It is observed that the maximum percent reduction achieved in the connected configuration is also similar to one patch

configuration which is 69%. After adding 81 patches on the plate, a black gap occurs in modes 5 and 6, which can be explained due to the fact that the patches cover the symmetric strain region of the modes 5 and 6, and their effect is canceled and adding more patches do not help in reducing the vibration amplitudes. **Fig. 5 -(ii)** shows much better performance when the patches are separately shunted, compared to the connected configuration. The percent reduction can be up to 79 % for all of the modes. It can be also observed that 49 patches would be sufficient to achieve this performance without a need for further increasing the number of patches.

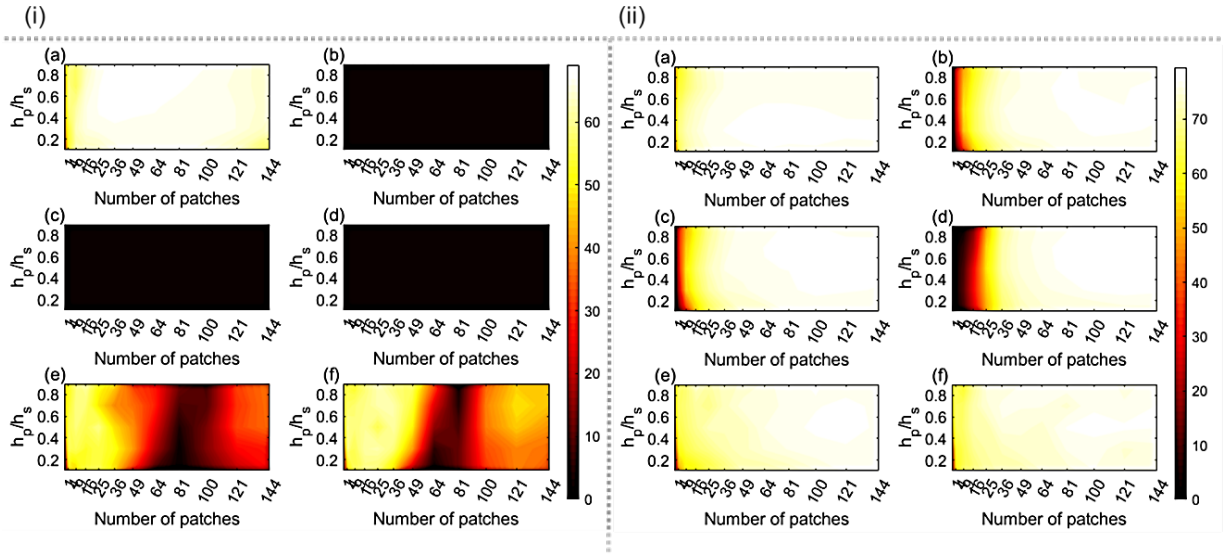

Fig. 5. (i) Percentage reduction achieved with multiple patches in a connected configuration: (a)First mode, (b)Second mode, (c)Third mode, (d) Fourth mode, (e) Fifth mode, and (f) Six mode , where the R values are consistent across all modes; (ii) Percentage reduction achieved with multiple patches in a separated configuration: (a) mode 1, (b) mode 2, (c) mode 3, (d) mode 4, (e) mode 5, and (f) mode 6, with R values uniform across all modes.

3.3 Multiple patches covering the same effective area: changing thickness and number of the patches

This section investigates the influence of the effective area of the patches and their sizes on shunt damping performance. **Fig. 6.** demonstrates the cases used in this section. Effective area is varied from $\frac{A_p}{A_s} = 0.01$ to $\frac{A_p}{A_s} = 0.75$ while the numbers of patches are increased. Then connected and separated configurations are compared.

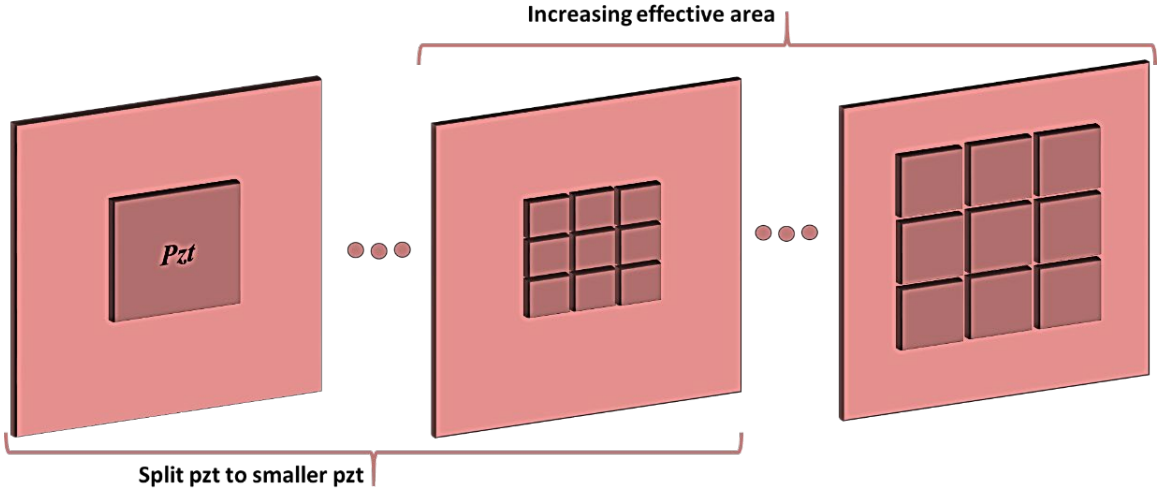

Fig. 6. Demonstration of splitting the effective area to multiple patches.

An effective area is the part of the host structure which is covered by all of the patches. For simplicity, numbers of the patches are increased from 1 to 36, all symmetric relative to the center of the plate. At each iteration, the average energy recovery performance $\overline{\text{ERP}}$ is assessed while the resistance value ranges from SC to OC. The same procedure is repeated at a different number of patches and effective area ratios. Fig. 7. represents the percent reduction for the connected and separated configurations, respectively. **Fig. 7 -(i)** shows the percent reduction for connected configuration when the effective area and

number of patches are changed. The ineffectiveness of the patches at modes 2, 3 and 4 can be observed when the effective area is near $\frac{A_p}{A_s} = 0.36$. The black gaps can be also observed on modes 5 and 6, which is again due to the symmetric nature of these modes and the cancelation effect. Shunt damping performance doesn't improve as the number of patches increase, because connected patches behave as a single patch when the effective area is kept constant. The maximum percent reduction is achieved only in the first mode which is 69 %. **Fig. 7-(ii)** shows the percent reduction on the separated configuration. Unlike the connected configuration, as the number of patches increases the percent reduction gets improved, so for the case of 1 patch configuration, the results are the same as **Fig. 6**. and it gets improved as the number of patches increases. For case $\frac{A_p}{A_s} = 0.36$, when the patches are separately shunted, the black region in **Fig. 7-(i)** reduces and it can be only seen in the region where the numbers of patches are low. The maximum percent reduction is 79% same as the separated configuration in the previous section.

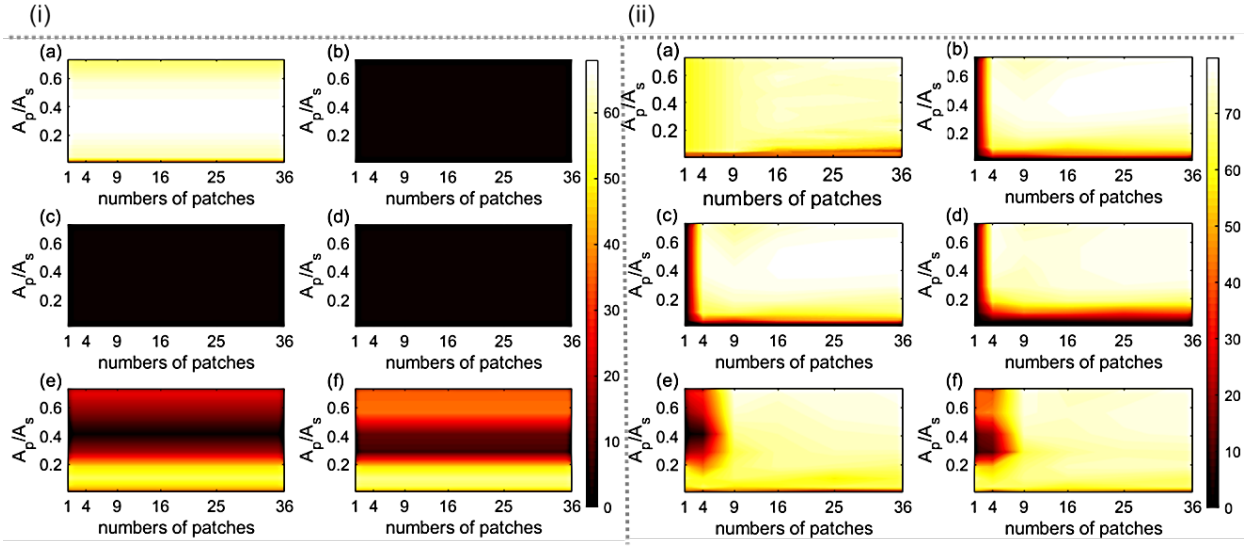

Fig. 7. (i) Percentage reduction achieved with multiple patches in a connected configuration with identical effective area, for the first six modes: (a-f) first to Six mode; the R values remain consistent across all modes. (ii) Percentage reduction achieved with multiple patches in a separated configuration with the same effective area, for the first six modes: (a-f) first to Sixth mode; the R values are uniform across all modes.

3.4 Optimization of shunt circuit resistance values

The plate dimensions are chosen because this patch can cover almost 90% of the plate and the effective area can be divided into 4, 9, 16 and 25 small patches. Excitation force is in the middle of the plate and the $\overline{\text{ERP}}$ is investigated. Initially, the optimization study is conducted only for the first mode and then repeated for the first three modes of the structure. There are two major results which are presented in Fig. 8.; optimum values of R and optimized values of R. The optimum values are obtained using the same procedure as in the previous section where R is swept from SC to OC and the same R values are used for all the patches. The optimized value will be the case when the patches have different R values and each one of them is swept from SC to OC. In a case when there are m patches and n variation of R values, the overall cases are in the order of m^n cases where, the computation cost is increasing as the number of patches increases. It can be shown that as the number of patches increases, the amplitude can be reduced further with the optimized R values. For the first mode, the optimized R values are near to the optimum values but as the number of patches increases, the distribution of the R values follows the strain mode shape of the first mode. The amplitude reduction can also be improved by adding more patches to the system. **Fig. 8.** includes the comparison between the cases of optimized and optimum values. **Table 1** illustrates the percentage reduction as the number of patches increases for both the optimal and optimized resistance values. It is noted that utilizing twenty-five patches results in a 3.3% enhancement when the resistance values are optimized for the first mode.

Table 1. Reduction of $\overline{\text{ERP}}$ amplitude

Number of patches	Percent Reduction for the case of optimum values	Percent Reduction for the case of optimized values	Improvement (%)
4	64.79	64.79	0.00
9	68.99	69.55	0.57
16	72.08	73.74	1.66
25	72.17	75.47	3.30

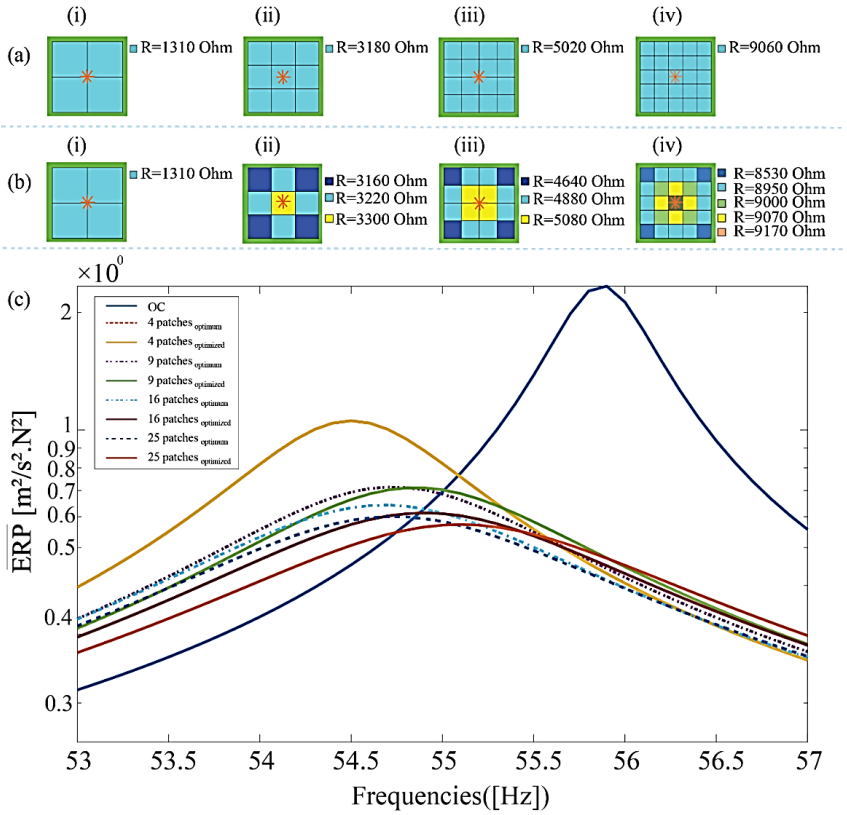

Fig. 8. R values distribution for cases (a) Optimum R values: (i) 4 patches, (ii) 9 patches, (iii) 16 patches, (iv) 25 patches; (b) Optimized R values: (i) 4 patches, (ii) 9 patches, (iii) 16 patches, (iv) 25 patches; (c) $\overline{\text{ERP}}$ for part (a) and (b). * Represent the force location.

Further investigation is done on modes 2 and 3 by optimizing the R values for each patch. **Table 2** lists the percent (%) improvements for the case of twenty-five patches for each mode. **Fig. 9** shows the similarities of the mode shapes and the R distribution pattern for the first three modes of the structure. There is also a significant improvement when the $\overline{\text{ERP}}$ reduction is also considered (see **Table 2**). It is observed that near the edges, R values get the lowest values.

Table 2. Reduction of $\overline{\text{ERP}}$ amplitude 5×5 patches case.

Modes	Optimum case	Optimized case	Differences (%)
2	66.98	76.74	9.76
3	61.80	73.47	11.67

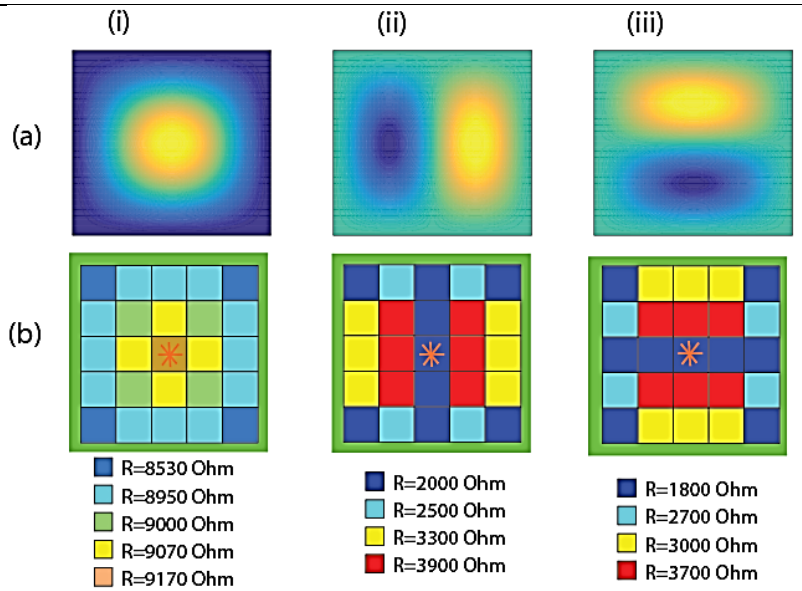

Fig. 9. Comparison cases of (a) mode shapes for the case of $\frac{A_p}{A_s} = 0.75$: (i) first mode, (ii) second mode, (iii) third mode; (b) resistor values for optimized case: (i) first mode, (ii) second mode, (iii) third mode.

Conclusion

This paper presents a new modeling approach dealing with piezoelectric patches considering they are shunt damped via different circuits, to showcase the efficiency, various considerations such as dimensions, ratio and locations are investigated. To achieve the model, Hamilton principles assumptions are studied and furthermore, Rayleigh-Ritz considerations are performed to achieve the modal and harmonic response. And finally, an optimization study is performed that examines how the arrangement of the shunt circuit can impact response of the initial three modes of the. It was demonstrated that the arrangement of the optimum resistor values mirrored the strain mode shapes of the targeted modes, simultaneously yielding an improvement of approximately 12% in the average energy recovery performance $\overline{\mathrm{ERP}}$ metric. Future studies can be conducted by adding more electrical circuit elements (i.e., Inductance) to the system and their design parameters can be optimized using a similar procedure. Nonetheless, the large number of variables would lead to a significant increase in case studies, resulting in extremely high computational costs. Therefore, different optimization techniques and modeling strategies could be investigated in future research to minimize these costs.

References

Acar, M. K., & Motlagh, P. L. (2024). A new framework for optimizing energy harvesting from smart composites integrated with piezoelectric patches utilizing lamination parameters. *Engineering Solid Mechanics*, *12*(2), 141–156.

Aghakhani, A., Lahe Motlagh, P., Bediz, B., & Basdogan, I. (2019). A general electromechanical model for plates with integrated piezo-patches using spectral-Tchebychev method. *Journal of Sound and Vibration*, *458*, 74–88.

Dekemele, K., Giraud-Audine, C., & Thomas, O. (2024). A piezoelectric nonlinear energy sink shunt for vibration damping. *Mechanical Systems and Signal Processing*, *220*, 111615.

Erturk, A., & Inman, D. J. (2009). An experimentally validated bimorph cantilever model for piezoelectric energy harvesting from base excitations. *Smart Materials and Structures*, *18*(2), 025009.

Erturk, A., & Inman, D. J. (2011). *Piezoelectric energy harvesting*. John Wiley & Sons.

Fleming, A. J., & Moheimani, S. O. R. (2003). Adaptive piezoelectric shunt damping. *Smart Materials and Structures*, *12*(1), 36.

Gardonio, P., & Rodrigues, G. K. (2024). Shunted piezoelectric patch adaptive vibration absorber set to maximise electric power absorption: A comparison between parallel and series RL-shunts. *Journal of Vibration and Control*, 10775463241246872.

Lahe Motlagh, P., Bediz, B., Alan, S., & Kefal, A. (2023). Analysis of smart laminated composites integrated with piezoelectric patches using spectral element method and lamination parameters. *Journal of Sound and Vibration*, *567*, 118063.

Liao, Y., Qian, F., Lo, Y.-C., & Shu, Y.-C. (2024). A study on the electrically induced damping in piezoelectric energy harvesting for broadband, high-performance power generation. *Energy Conversion and Management*, *307*, 118374.

Ma, S., Zhang, Y., Zhuang, X., Wang, D., Chen, S., & Liu, H. (2024). Frequency tuning and automatic frequency tracking of shunted piezoelectric transducers. *Ultrasonics*, *141*, 107318.

Motlagh, P. L., Aghakhani, A., & Basdogan, I. (2018). Passive vibration control of a plate via piezoelectric shunt damping with FEM and ECM. *Smart Materials and Nondestructive Evaluation for Energy Systems IV*, *10601*, 8–15.

Motlagh, P. L., Anamagh, M. R., Bediz, B., & Basdogan, I. (2021). Electromechanical analysis of functionally graded panels with surface-integrated piezo-patches for optimal energy harvesting. *Composite Structures*, *263*, 113714.

Motlagh, P. L., Bediz, B., & Basdogan, I. (2020). A spectral Tchebychev solution for electromechanical analysis of thin curved panels with multiple integrated piezo-patches. *Journal of Sound and Vibration*, *486*, 115612.

Muthalif, A. G. A., & Wahid, A. N. (2021). Optimal piezoelectric shunt dampers for non-deterministic substructure vibration control: Estimation and parametric investigation. *Scientific Reports*, *11*(1), 4642.

Paixão, J., Foltête, E., Sadoulet-Reboul, E., Chevallier, G., & Cogan, S. (2024). Self-adaptive piezoelectric vibration absorber with semi-passive tunable resonant shunts. *Journal of Sound and Vibration*, *583*, 118424.

Richardt, J. D., Lossouarn, B., Høgsberg, J., & Deü, J.-F. (2024). Calibration of multiple shunted piezoelectric transducers with correction for residual modes and shunt interactions. *Journal of Vibration and Control*, 10775463241241838.

Yaw, Z., Zhou, W., & Lim, C. W. (2024). Adaptive control on flexural waves by a piezoelectric-based elastic metasurface with hybrid shunting circuits. *Mechanics of Advanced Materials and Structures*, *31*(15), 3348–3355.

Zhang, L., Li, M., Sun, X., & Cheng, W. (2024). A nonlinear piezoelectric shunt absorber with tunable piecewise linear negative capacitance. *Smart Materials and Structures*, *33*(8), 085037.